

# Comprehensive examination of the elastic scattering angular distributions of $^{10}\text{C}+^4\text{He}$ , $^{27}\text{Al}$ , $^{58}\text{Ni}$ and $^{208}\text{Pb}$ using various potentials

M. N. El-Hammamy

*Physics Department, Faculty of Science, Damanhur University, Damanhur, Egypt.*

Awad A. Ibraheem

*Physics Department, King Khalid University, Abha, Saudi Arabia.*

*Physics Department, Al-Azhar University, Assiut Branch, Assiut 71524, Egypt.*

M. El-Azab Farid

*Physics Department, Assiut University, Assiut, 71516, Egypt.*

E. F. Elshamy

*Physics Department, King Khalid University, Abha, Saudi Arabia.*

Sh. Hamada

*Physics Department, Faculty of Science, Tanta University, Tanta, Egypt.*

Received 06 July 2022; accepted 22 August 2022

The recently measured elastic scattering angular distributions for  $^{10}\text{C} + ^4\text{He}$ ,  $^{10}\text{C} + ^{27}\text{Al}$ ,  $^{10}\text{C} + ^{58}\text{Ni}$  and  $^{10}\text{C} + ^{208}\text{Pb}$  nuclear systems are investigated in the current study using various potentials based on phenomenological, semi microscopic as well as microscopic approaches. The implemented potentials are: optical potential, double folding potentials based on both Sao Paulo and CDM3Y6 interactions with and without taking into account the effect of the rearrangement term, as well as the cluster folding potential. The cluster nature of  $^{10}\text{C}$  as a core of  $^9\text{B}$  with a valence proton orbiting this core is applied to generate the cluster folding potentials for the different considered systems. The concerned experimental data is fairly reproduced with all the aforementioned potentials.

**Keywords:** Elastic scattering; Sao Paulo potential; phenomenological potential; cluster folding; dynamical polarization potential.

DOI: <https://doi.org/10.31349/RevMexFis.69.031201>

## 1. Introduction

For a long time, the study of nuclear potentials of elastically (inelastically) scattered interacting systems has been a hot issue in the field of nuclear physics. Several theoretical studies have been carried out to determine nuclear potentials in order to examine the nucleon-nucleon ( $NN$ ) interactions, the sensitivity of different density distribution forms as well as the structure of interacting nuclei [1-6]. For years, a significant progress was made in the computational tools used in determining nuclear potentials. To characterize the elastic scattering of a projectile nucleus from a target nucleus, the phenomenological optical model (OM) is commonly used. It is recognized by its complex potential form in terms of real and imaginary volume parts, each of Woods-Saxon (WS) shape. One of the most popular approaches [1] for evaluating the real part of the nucleus (nucleon)-nucleus optical potential (OP) in semi-microscopic interpretation of experimental data is the folding model (FM), which comes in two types: single folding (SF) and double folding (DF). Its ingredients, notably the projectile and target density distributions as well as effective  $NN$  interaction potential have been thoroughly examined for numerous nuclear systems. Theoretical calculations or experimental data can be used to produce these density

distributions. The most widely employed effective  $NN$  interactions are the so called density independent Michigan 3 Yukawa terms (M3Y) and single Yukawa term (S1Y) [7] or their density dependent versions [1,8]. Like the conventional FM, the cluster folding model (CFM) computes the real OP, but with the effective cluster-cluster interaction and the clustered density distributions [9-12]. This treatment might highlight the relevance of clusters in nuclei.

In this regard, Satchler and coworkers [13,14] in examining the mechanism of heavy ion (HI) elastic scattering highlighted the usefulness of employing density independent M3Y and S1Y  $NN$  interaction potentials in DF calculations. A successive analysis by using  $JLM$  potential developed by Jeukenne, Lejuene, and Mahaux is done by Farid and Hassanian [15-17]. Another applicability of DF calculations with different types of  $NN$  interaction potentials are: density dependent CDM3Y6 [18,19], CDM3Y6-RT proposed by Khoa [20] which takes into account the effect of rearrangement term (RT), velocity dependent Sao Paulo potential (SPP), and independent Brazilian nuclear potential (BNP) given by Chammon *et al.* [21,22] and presented in Refs. [23-26]. For  $^{11}\text{Li}$  nucleus, Behairy *et al.* [27] discussed the preferable density distribution forms among cluster-orbital shell model approximation (COSMA), Semi-phenomenological

(SP), Hartree–Fock (HF) as well as M. Anwar *et al.* examined the cluster model (CM) density for  $^8\text{B}$  [28] and two parameters-Fermi (2pF), Gaussian–Oscillator (GO), Gaussian (G) for  $^6\text{Li}$  [29] to produce the best fit for the experimental data. On the other hand, Li-Yuan Hu *et al.* [30] constructed the Cluster folding potential (CFP) of  $^6\text{He}$  and  $^6\text{Li}$  to analyze their elastic scattering data from  $^{12}\text{C}$  at various energies. Hamada *et al.* [32] analyzed  $^6\text{Li}$  elastic scattering from  $^{16}\text{O}$  in the energy range of 13-50 MeV using the CF potential in comparison to DF potential. Another pertinence of this model is conferred in Refs. [33-35]. As seen above, for different projectiles, a suitable description of the experimental data might be produced by employing different combinations of densities in addition to appropriate effective  $NN$  potentials.

Besides, the breakup threshold anomaly (BTA), a scattering process related phenomenon, has been probed over the years [36,37]. In the case of weakly bound nuclei, it is characterized by an increase of the imaginary potential part as the incident energy declines towards the coulomb barrier energy. The energy dependence of optical potentials derived by fitting the elastic scattering data of many systems including  $^6\text{Li}$ ,  $^6\text{He}$ ,  $^7\text{Li}$ ,  $^7\text{Be}$  and  $^8\text{B}$  projectiles has shown this trend [38-40]. In case of tightly bound nuclei, however, the imaginary potential behavior is reversed, resulting in the well-known threshold anomaly (TA) phenomenon. At close or sub-barrier energies the imaginary potential dramatically declines, whereas the real part forms a “bell-shaped maximum” [14,41,42]. To put it in another way, BTA is the absence of TA at the coulomb barrier. Both the real and imaginary potentials are nearly energy independent at higher energies. Concerning this issue, V. Guimarães *et al.* [43] conducted a phenomenological analysis on the elastic scattering of different projectiles; tightly-bound ( $^{10}\text{Be}$ ,  $^{10}\text{B}$ ,  $^{10}\text{C}$ ,  $^{11}\text{B}$ ,  $^{12}\text{C}$ ,  $^{16}\text{O}$ ), weakly-bound ( $^6\text{Li}$ ,  $^7\text{Li}$ ,  $^8\text{Li}$ ,  $^9\text{Be}$ ) and exotic ( $^6\text{He}$ ,  $^8\text{B}$ ,  $^{11}\text{Be}$ ) on  $^{58}\text{Ni}$  and  $^{64}\text{Zn}$  targets at energies close to the barrier. Furthermore, Awad and M. Aygun [44] applied dynamic polarization potential (DPP) in order to account for the coupling to the breakup channel of the projectile  $^{11}\text{Be}$  scattering from  $^{64}\text{Zn}$  at center of mass energy 24.5 MeV.

In this paper, we extend the investigation to the case of the  $^{10}\text{C}$  projectile, compare the results to those obtained by others, assess the sensitivity of the result to the projectile density used and demonstrate whether BTA is presented in different implemented potentials on elastic scattering data. Our results might have implications for future study in the same subject.

$^{10}\text{C}$  is a proton rich nucleus with binding energies 4.007, 3.821 and 5.101 MeV for its three probable decay channels;  $^9\text{B} + \text{p}$ ,  $^8\text{Be} + \text{p} + \text{p}$  and  $^6\text{Be} + \alpha$ , respectively. This nucleus can be regarded to have  $\alpha + \alpha + \text{p} + \text{p}$  configuration because  $^8\text{Be}$ ,  $^9\text{Be}$  and  $^6\text{Be}$  are all unbound systems. Actually,  $^{10}\text{C}$  is the only four body nucleus known to possess the Borromean-like features. Brunnian (Super-Borromean) nucleus [45,46] is the name given to this type of nuclei. Both experimental and theoretical nuclear physicists are interested in this exotic configuration. Many reactions involving  $^{10}\text{C}$  have been thoroughly investigated using both experimental and theoretical

methods. Furuno *et al.* [47], for example published elastic and inelastic scattering measurements of  $^{10}\text{C}$  on  $^4\text{He}$  reaction at 68 MeV/n as well as thorough analysis. At 35.5 MeV, V. Guimarães *et al.* [48] measured and examined the elastic scattering cross sections of  $^{10}\text{C}$  on  $^{58}\text{Ni}$ . Measurements and investigation of the elastic scattering of  $^{10}\text{C}$  on  $^{27}\text{Al}$  were executed by Aguilera *et al.* [49] at 29.1 MeV. Yang *et al.* [50] performed elastic measurements of  $^{10}\text{C}$  on  $^{208}\text{Pb}$  at 226 and 256 MeV, and Linares *et al.* at 66 MeV [51]. What is more, theoretical descriptions of the experimental data were reported by authors.

The methodologies used in the calculations are described in the next section. Section 3 contains the results and discussions. The summary and conclusions extracted from the current study are presented in Sec. 4.

## 2. Theoretical formalism

The available experimental elastic scattering angular distributions for the  $^{10}\text{C} + ^4\text{He}$ ,  $^{10}\text{C} + ^{27}\text{Al}$ ,  $^{10}\text{C} + ^{58}\text{Ni}$  and  $^{10}\text{C} + ^{208}\text{Pb}$  systems at different energies [47-51] are subjected to a detailed analysis using different phenomenological, semi-microscopic, and microscopic potentials in order to observe the weak nature of the  $^{10}\text{C}$  projectile on the elastic scattering data.

The nuclear potential is a fundamental ingredient in the study of nuclear reactions. The optical model potential (OMP) is widely adopted to describe the interaction of nuclear collisions phenomenologically. The utilized central potential consists of Coulomb part, as well as nuclear part of real and imaginary volume terms, each of (WS) shape. For simplicity and its little influence, the spin orbit potential ( $V_{SO}$ ) is excluded. The used central potential has the following form:

$$U(R) = V_C(R) - V_0 \left[ 1 + \exp\left(\frac{R - R_V}{a_V}\right) \right]^{-1} - iW_0 \left[ 1 + \exp\left(\frac{R - R_W}{a_W}\right) \right]^{-1},$$

$$R_i = r_i(A_T^{1/3}), \quad i = V, W. \quad (1)$$

The  $V_C(R)$  is the Coulomb potential between two charged spheres representing the projectile and target nuclei, and takes the following form:

$$V_C(R) = \frac{Z_1 Z_2 e^2}{2R_C} \left( 3 - \frac{R^2}{R_C} \right) \quad \text{for } R \leq R_C, \quad \text{or}$$

$$= \frac{Z_1 Z_2 e^2}{R_C} \quad \text{for } R \geq R_C. \quad (2)$$

In the semi-microscopic form, the optical nucleus-nucleus potential used in the present work is given by:

$$U(R) = V_C(R) - N_R V^{DF}(R) - iW_V(R), \quad (3)$$

where  $V^{DF}(R)$  is the real DF potential, and  $N_R$  is the renormalization factor for the implemented real microscopic DF potential which is allowed to be freely changed till the best agreement between experimental data and theoretical calculations is reached. The real DF potential is calculated as,

$$V^{DF}(R) = \iint \rho_P(\vec{r}_1) \rho_T(\vec{r}_2) v_{NN}(S) d\vec{r}_1 d\vec{r}_2, \quad (4)$$

here  $\rho_P(r_1)$ ,  $\rho_T(r_2)$  are the nuclear matter density of the projectile and the target, respectively. While  $v_{NN}(S)$  is the effective  $NN$  interaction between two nucleons,  $S = \vec{R} - \vec{r}_1 + \vec{r}_2$ , and  $W_V(R)$  is the phenomenological imaginary potential having a WS shape,

$$W(R) = \frac{W_0}{1 + \exp\left[\frac{R-R_W}{a_W}\right]}, \quad (5)$$

where  $W_0$ ,  $R_W$  and  $a_W$  are the depth, radius and diffuseness of the potential, respectively.  $R_W = r_W(A_P^{1/3} + A_T^{1/3})$ , where,  $A_P$ ,  $A_T$  are the projectile and target mass number.

## 2.1. Nuclear matter density distributions

For the  $^{10}\text{C}$  nucleus, three different densities distributions are used. The first one is obtained from the theoretical Dirac-Hartree-Bogoliubov (DHB) model that used in the REGINA code [22]. This density yields a root mean square radius of 2.66 fm. The second density distribution is taken in the semi-phenomenological density (SPH) form, where the total matter density distribution can be taken as,

$$\rho(r) = \rho_n(r) + \rho_p(r). \quad (6)$$

Both neutrons and protons density distributions can be written in the following expression [2,3],

$$\rho_i(r) = \frac{\rho_i^0}{1 + \left[ \left( \frac{1 + \left(\frac{r}{R}\right)^2}{2} \right)^{\alpha_i} \left[ \exp\left(\frac{(r-R)}{a_i}\right) + \exp\left(\frac{-(r+R)}{a_i}\right) \right] \right]}, \quad (7)$$

where  $p$  stands for the protons and  $n$  for neutrons,  $i = p, n$ . The central densities  $\rho_p^0$  and  $\rho_n^0$  are determined from the normalization conditions:

$$4\pi \int \rho_n(r) r^2 dr = N, \quad (8)$$

$$4\pi \int \rho_p(r) r^2 dr = Z, \quad (9)$$

where  $N(Z)$  is the total number of neutrons (protons) in the nucleus and the other parameters ( $\alpha_i$ ,  $a_i$ ) can be determined in detail through Refs. [52,53]. Finally, the third density distribution form is that deduced using the Argonne v18 two-nucleon and Urbana X three-nucleon potentials (AV18+UX) in a realistic Variational Monte Carlo (VMC) wave function [54]. The radial shape of the considered different types of the density distributions of  $^{10}\text{C}$  are shown in Fig. 1, in linear and logarithmic scale.

At  $r = 0$ , the VMC density distribution differs from the two other densities, which suggests that there might be a problem with numeric convergence. The elastic scattering cross sections of  $^{10}\text{C}$  projectile by four different targets ( $^4\text{He}$ ,  $^{27}\text{Al}$ ,  $^{58}\text{Ni}$  and  $^{208}\text{Pb}$ ) have been examined. With this goal, we used the numerical tables of the density distributions generated from REGINA code [22] for  $^4\text{He}$ ,  $^{27}\text{Al}$ ,  $^{58}\text{Ni}$  and  $^{208}\text{Pb}$  targets, which yield a root mean square radius (rms) = 2.17, 3.13, 3.78 and 5.64 fm, respectively.

## 2.2. The $NN$ effective interactions

Based upon the M3Y interactions which is designed to reproduce the G-matrix elements for Paris and Reid [7,55] effective  $NN$  interactions, CDM3Y6 version of the M3Y effective  $NN$  interaction is used in addition to the CDM3Y6-RT interaction that recently modified by introducing the RT [20]. The full CDM3Y6 interaction form is defined as [18],

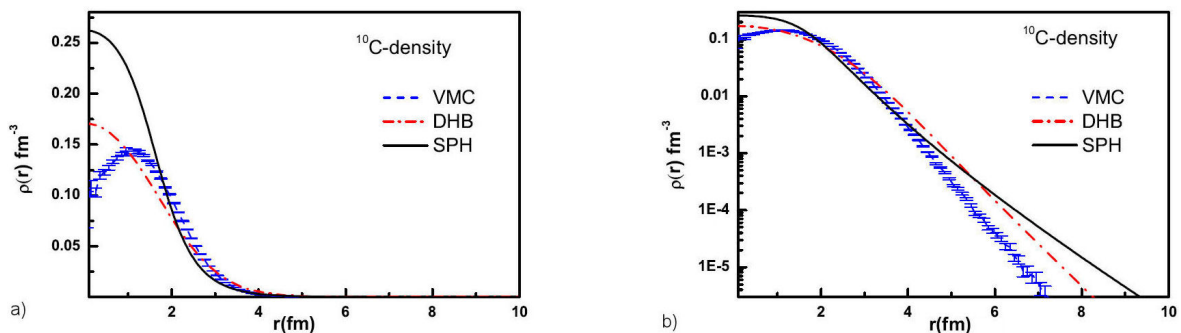


FIGURE 1. The densities of  $^{10}\text{C}$  as a) linear and b) logarithmic scales with errors in the VMC calculations.

$$v_{D(E_x)}(\rho, s) = g(E) F(\rho) v_{D(E_x)}(s), \quad (10)$$

$$v_D(s) = \left[ 11062 \frac{e^{-4s}}{4s} - 2538 \frac{e^{-2.5s}}{2.5s} \right] \text{ MeV}, \quad (11)$$

and the knock-on exchange part in the infinite-range exchange is

$$v_{Ex}(s) = \left[ -1524 \frac{e^{-4s}}{4s} - 518.8 \frac{e^{-2.5s}}{2.5s} - 7.847 \frac{e^{-0.7072s}}{0.7072s} \right] \text{ MeV} \quad (12)$$

with the function  $F(\rho)$  is written as [18,19],

$$F(\rho) = 0.2658 [1 + 3.8033 \exp(-1.41\rho) - 4.0\rho], \quad (13)$$

while  $g(E)$  is the energy dependent factor given as [18],

$$g(E) = [1 - 0.003 (E/A)], \quad (14)$$

For reproducing the saturation properties of symmetric nuclear matter (NM) in the standard HF calculation and to have a reliable density dependent interaction for use at different energies (the high-momentum part of the HF single-nucleon potential), the modified CDM3Y6 interaction (CDM3Y6-RT) with the RT contribution has been carried out. The density dependence of  $\Delta F(\rho)$  obtained from the exact expression of the RT given as [18]:

$$\Delta F(\rho) = 1.5 [\exp(-0.833\rho) - 1], \quad (15)$$

On the other hand, we use the SPP, where the radial and energy dependence is written in the following [22],

$$V_N(R, E) = V_F(R) e^{-\frac{4V^2}{c^2}}, \quad (16)$$

$$V^2(R, E) = \frac{2}{\mu} [E - V_C(R) - V_N(R, E)], \quad (17)$$

where  $V$  is the nuclei's local relative velocity and  $C$  is the speed of light. The nuclear densities obtained from the DHB model and the (SPP) are calculated using the REGINA code [22].

### 2.3. Cluster folding optical model (CFOM)

According to the appreciable  ${}^9\text{B} + \text{p}$  cluster structure of  ${}^{10}\text{C}$  which appears at energy of 4.007 MeV, it is interesting to analyze the considered systems:  ${}^{10}\text{C} + {}^4\text{He}$ ,  ${}^{10}\text{C} + {}^{27}\text{Al}$ ,  ${}^{10}\text{C} + {}^{58}\text{Ni}$ , and  ${}^{10}\text{C} + {}^{208}\text{Pb}$  using real microscopic potential constructed based on (CF) procedure. The main ingredients for generating the  ${}^{10}\text{C} + \text{Target}$  ( ${}^4\text{He}$ ,  ${}^{27}\text{Al}$ ,  ${}^{58}\text{Ni}$  and  ${}^{208}\text{Pb}$ ) CF

potentials are:  ${}^9\text{B} + \text{target}$  and  $\text{p} + \text{target}$  potentials at appropriate energies as expressed in Eq. (18)

$$V^{CF}(\mathbf{R}) = \int \left[ V_{{}^9\text{B}-\text{Target}} \left( \mathbf{R} - \frac{1}{10}\mathbf{r} \right) + V_{\text{p}-\text{Target}} \left( \mathbf{R} + \frac{9}{10}\mathbf{r} \right) \right] |\chi_{{}^9\text{B}-\text{p}}(\mathbf{r})|^2 d\mathbf{r}, \quad (18)$$

in addition to the wave function  $\chi_{{}^9\text{B}-\text{p}}(\mathbf{r})$  of the cluster which describes the  ${}^9\text{B}$  and  $\text{p}$  relative motion in the ground state of  ${}^{10}\text{C}$ . The  ${}^9\text{B} + \text{p}$  bound state form factor represents a 1S state in a real WS potential of radius 1.83 fm and diffuseness of 0.7 fm, the potential depth is allowed to be change till the binding energy of the cluster (4.007 MeV) is achieved, the parameter ISC in the implemented FRESCO code [56] permit such adjustment. Of course, the same WS potential parameters for the bound state ( ${}^{10}\text{C} \rightarrow {}^9\text{B} + \text{p}$ ) were used in preparing CFP potential for all the considered systems. While, suitable  $V_{{}^9\text{B}-\text{Target}}$  and  $V_{\text{p}-\text{Target}}$  potentials were prepared and chosen as follow:

1. For  ${}^{10}\text{C} + {}^4\text{He}$  system, the considered data is at  $E({}^{10}\text{C}) = 680$  MeV. So, the required potentials are  ${}^9\text{B} + {}^4\text{He}$  at  $E = 9/10 \times 680 = 612$  MeV and  $\text{p} + {}^4\text{He}$  at  $E = 1/10 \times 680 = 68$  MeV. As there is no experimental data for the  ${}^9\text{B} + {}^4\text{He}$  channel, the  ${}^9\text{B} + {}^4\text{He}$  potential is prepared using the SPP within the framework of REGINA code. The inherited density distributions for  ${}^{10}\text{C}$  and  ${}^4\text{He}$  in this code were implemented, and the renormalization factor for the real SPP ( $N_{RSPP}$ ) was taken by default 1.0. On the other side, the  $\text{p} + {}^4\text{He}$  potential at  $E = 55$  MeV [57] was utilized, as it is the closest existed data to  $\text{p} + {}^4\text{He}$  at  $E = 68$  MeV found in literature.
2. For  ${}^{10}\text{C} + {}^{27}\text{Al}$  system, the considered data is at  $E({}^{10}\text{C}) = 29.1$  MeV. Hence, the required potentials are  ${}^9\text{B} + {}^{27}\text{Al}$  at  $E = 9/10 \times 29.1 = 26.19$  MeV and  $\text{p} + {}^{27}\text{Al}$  at  $E = 1/10 \times 29.1 = 2.91$  MeV. The  ${}^9\text{B} + {}^{27}\text{Al}$  potential is prepared using the SPP within the framework of REGINA code. The  $N_{RSPP}$  was fixed at 1.0. While, the  $\text{p} + {}^{27}\text{Al}$  potential at  $E = 9.1$  MeV [58,59] was utilized (closest existed data to  $\text{p} + {}^{27}\text{Al}$  at  $E = 2.91$  MeV).
3. For  ${}^{10}\text{C} + {}^{58}\text{Ni}$  system, the considered data is at  $E({}^{10}\text{C}) = 35.3$  MeV. Consequently, the required potentials are:  ${}^9\text{B} + {}^{58}\text{Ni}$  at  $E = 9/10 \times 35.3 = 31.77$  MeV and  $\text{p} + {}^{58}\text{Ni}$  at  $E = 1/10 \times 35.3 = 3.53$  MeV. Real SPP created utilizing REGINA code was implemented for the  ${}^9\text{B} + {}^{58}\text{Ni}$  channel using  $N_{RSPP} = 1.0$ . The  $\text{p} + {}^{58}\text{Ni}$  potential at  $E = 6.9$  MeV [58] was utilized.
4. For  ${}^{10}\text{C} + {}^{208}\text{Pb}$  system, the considered data are at energies  $E({}^{10}\text{C}) = 66, 226, \text{ and } 256$  MeV. The most suit-

TABLE I. The best fit parameters for  $^{10}\text{C} + ^4\text{He}$ ,  $^{27}\text{Al}$  and  $^{58}\text{Ni}$  systems extracted from the different implemented potentials and densities combination.

Target/ Energy	Density type	Potential	$V_o$ (MeV)/ $N_R$	$r_V$ (fm)	$a_V$ (fm)	$W_o$ (MeV)	$r_W$ (fm)	$a_W$ (fm)	$J_R$ (MeV.fm <sup>3</sup> )	$J_I$ (MeV.fm <sup>3</sup> )	$\sigma_R$ (mb)	$\chi^2$
$^4\text{He}/68$ MeV/n		WS	14.81	1.378	0.871	24.14	1.243	0.291	272.29	264.45	796.8	0.49
	DHB	CDM3Y6	0.81			6.36	1.556	1.183	312.68	185.25	1227	6.09
		CDM3Y6-RT	0.98			6.44	1.516	1.355	317.12	192.59	1307	7.45
	DHB	SP	1.01			6.33	1.639	0.659	287.63	170.21	1024	2.94
	SPh	CDM3Y6	0.87			6.24	1.605	0.957	307.12	176.94	1132	3.93
		CDM3Y6-RT	1.14			6.36	1.563	1.161	315.73	184.96	1220	5.69
	VMC	CDM3Y6	0.82			6.39	1.584	1.048	303.66	182.34	1176	4.03
		CDM3Y6-RT	1.02			6.47	1.554	1.182	308.15	187.66	1235	4.99
	DHB	CF	0.89			6.30	1.631	0.723	289.67	170.86	1043	2.91
$^{27}\text{Al}/29.1$ MeV		WS	45.0	1.292	0.467	15.25	1.466	0.345	216.14	106.32	958.9	17.95
	DHB	CDM3Y6	0.87			90.04	1.434	0.169	424.30	567.26	835.3	19.49
		CDM3Y6-RT	0.87			98.73	1.419	0.168	353.23	602.38	812.1	19.24
	DHB	SP	1.25			47.93	1.403	1.001	535.49	281.5	682.5	17.10
	SPh	CDM3Y6	0.87			94.91	1.391	0.165	381.05	545.7	765.7	19.06
		CDM3Y6-RT	0.87			94.37	1.377	0.162	293.92	525.55	737.2	18.67
	VMC	CDM3Y6	1.10			81.01	1.413	0.129	507.14	486.63	735.3	17.79
		CDM3Y6-RT	1.06			67.78	1.403	0.120	395.40	398.58	704.4	17.39
	DHB	CF	1.00			80.43	1.382	0.125	438.88	452.91	683.9	17.21
$^{58}\text{Ni}/35.3$ MeV		WS	48.53	1.530	0.180	10.36	1.483	0.219	275.59	53.59	637.8	27.47
	DHB	CDM3Y6	0.62			49.00	1.480	0.200	282.76	252	526.8	19.17
		CDM3Y6-RT	0.65			49.00	1.480	0.200	240.74	252.71	525.7	18.97
	DHB	SP	1.15			40.00	1.480	0.200	480.97	205.87	505.8	17.68
	SPh	CDM3Y6	1.00			49.00	1.480	0.200	514.40	252.71	538.0	20.46
		CDM3Y6-RT	1.00			49.00	1.480	0.200	378.86	252.71	531.2	19.48
	VMC	CDM3Y6	0.95			55.00	1.481	0.220	410.11	283.94	548.1	19.19
		CDM3Y6-RT	0.98			58.00	1.481	0.220	332.57	299.43	547.1	18.59
	DHB	CF	1.00			55.00	1.481	0.220	423.66	283.94	545.8	18.71

able potential for  $^9\text{B} + ^{208}\text{Pb}$  channel at  $E = 9/10 \times 256 = 230.4$  MeV and  $\text{p} + ^{208}\text{Pb}$  at  $E = 1/10 \times 256 = 25.6$  MeV. The SPP for  $^9\text{B} + ^{208}\text{Pb}$  channel at  $E = 230.4$  was created utilizing REGINA code with  $N_{RSP} = 1.0$ . The  $\text{p} + ^{208}\text{Pb}$  potential at  $E = 26.3$  MeV [58, 60] was utilized in generating the  $^{10}\text{C} + ^{208}\text{Pb}$  CFP.

The created real CF potential in addition to a phenomenological WS imaginary potential, the so called the cluster folding optical model (CFOM), was applied to fit the considered data. Within the framework of CFOM, the following potential form Eq. (19) was adopted, where  $N_R$  is the renormalization factor for the real CF potential.

$$U(R) = V_C(R) - N_R V^{CF}(R) - iW_0 \left[ 1 + \exp\left(\frac{r - R_W}{a_W}\right) \right]^{-1}. \quad (19)$$

After that, the elastic-scattering differential cross sections generated by the phenomenological WS potentials and the semi-microscopic potentials are calculated by using HIOPTM-94 code [61] and compared with the experimental data as shown later in Figs. 4–9. The quality of fitting and hence the optimal potential parameters were obtained by minimizing the  $\chi^2$  value which defines the deviation between experimental data and calculations, and defined as follow:

$$\chi^2 = \frac{1}{N} \sum_{i=1}^N \left( \frac{\sigma(\theta_i)^{\text{cal}} - \sigma(\theta_i)^{\text{exp}}}{\Delta\sigma(\theta_i)} \right)^2. \quad (20)$$

The  $\sigma(\theta_i)^{\text{exp}}$  and  $\sigma(\theta_i)^{\text{cal}}$  are the experimental and calculated differential cross sections,  $\Delta\sigma(\theta_i)$  is the relative uncertainty in experimental data.

For semi-microscopic analysis, searches are carried out on four parameters, the real renormalization factor  $N_R$ , in

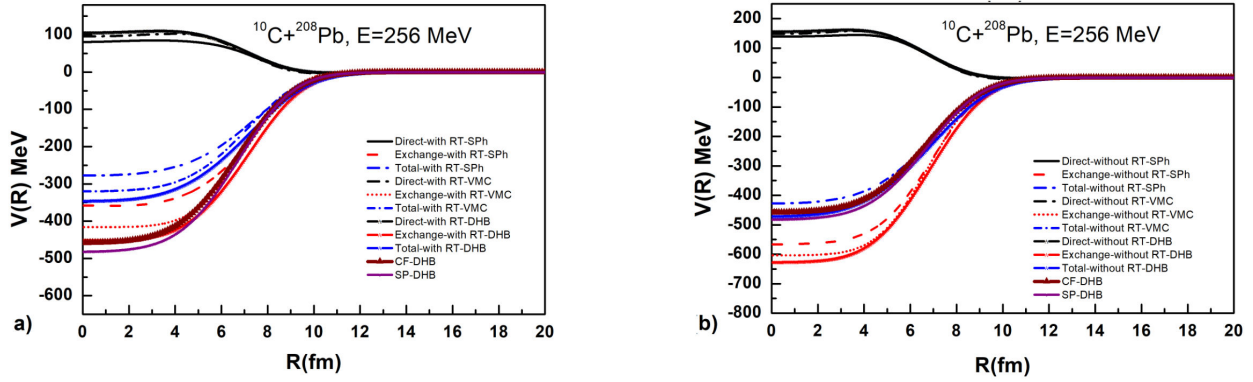


FIGURE 2. The obtained real microscopic potential for  $^{10}\text{C} + ^{208}\text{Pb}$  at  $E = 256$  MeV using CDM3Y6 interaction with (upper panel) and without rearrangement term (RT) (lower panel) utilizing three different densities; SPh, VMC and DHB for  $^{10}\text{C}$  as well as the CF and SP interaction potentials with DHB density.

TABLE II. TSame as Table 1 but for  $^{10}\text{C} + ^{208}\text{Pb}$  system.

Target/ Energy	Density type	Potential	$V_o$ (MeV) / $N_R$	$r_V$ (fm)	$a_V$ (fm)	$W_o$ (MeV)	$r_W$ (fm)	$a_W$ (fm)	$J_R$ (MeV.fm <sup>3</sup> )	$J_I$ (MeV.fm <sup>3</sup> )	$\sigma_R$ (mb)	$\chi^2$
$^{208}\text{Pb}/66$ MeV		WS	44.19	1.473	0.251	12.19	1.604	0.139	150.79	53.48	793.20	2.62
	DHB	CDM3Y6	0.77			59.74	1.520	0.225	334.21	223.72	763.6	3.45
		CDM3Y6-RT	0.78			48.25	1.520	0.222	272.04	180.56	742.5	3.32
	DHB	SP	1.17			13.390	1.579	0.149	473.68	56.11	739.9	2.75
	SPh	CDM3Y6	0.88			46.09	1.511	0.221	344.66	169.38	717.9	3.39
		CDM3Y6-RT	0.89			35.77	1.508	0.217	257.63	130.77	688.3	3.27
	VMC	CDM3Y6	0.71			55.98	1.484	0.281	282.03	195.22	714.5	2.56
		CDM3Y6-RT	0.73			55.83	1.483	0.281	211.96	194.56	714.4	2.55
	DHB	CF	0.88			68.26	1.480	0.258	309.20	236.14	703.9	2.96
$^{208}\text{Pb}/226$ MeV		WS	233.04	0.797	1.061	10.18	1.419	0.246	158.83	31.06	3133	0.94
	DHB	CDM3Y6	0.52			51.03	1.342	0.226	203.38	131.67	3023	0.98
		CDM3Y6-RT	0.52			51.03	1.337	0.262	164.31	130.34	3070	0.99
	DHB	SP	1.04			51.02	1.333	0.278	381.15	129.33	3091	1.00
	SPh	CDM3Y6	0.63			51.18	1.341	0.188	225.99	131.51	2938	0.94
		CDM3Y6-RT	0.67			51.17	1.343	0.209	174.69	132.09	2986	0.94
	VMC	CDM3Y6	1.15			50.96	1.262	0.513	405.16	111.50	3273	1.08
		CDM3Y6-RT	1.15			50.96	1.254	0.539	311.68	109.81	3296	1.10
	DHB	CF	0.89			51.10	1.351	0.170	315.89	134.09	2952	0.95
$^{208}\text{Pb}/256$ MeV		WS	307.37	0.743	0.895	5.49	1.474	0.176	163.49	18.75	3264	0.67
	DHB	CDM3Y6	0.48			112.19	1.304	0.202	184.71	265.32	3001	1.66
		CDM3Y6-RT	0.49			112.19	1.298	0.222	152.76	261.56	3020	1.66
	DHB	SP	0.99			116.39	1.299	0.221	356.13	272.01	3035	1.58
	SPh	CDM3Y6	0.48			112.19	1.245	0.315	168.05	232.18	3006	1.56
		CDM3Y6-RT	0.48			112.19	1.210	0.365	122.43	214.13	2970	1.41
	VMC	CDM3Y6	0.96			112.19	1.172	0.476	332.02	196.48	3098	1.22
		CDM3Y6-RT	0.96			112.19	1.150	0.518	254.07	187.01	3108	1.15
	DHB	CF	0.87			112.19	1.337	0.124	307.44	285.32	2954	1.77

addition to the three imaginary WS parameters for each case and are listed in Tables I and II. Moreover, the searched six WS parameters for real and imaginary potentials within phenomenological analysis are included in the same tables along with the values of the volume integrals per pair of interacting nucleons for the real ( $J_R$ ) and imaginary parts ( $J_I$ ), respectively, the absorption reaction cross-section ( $\sigma_R$ ), and the best-fit  $\chi^2$  values. In the succeeding section, we represent a detailed discussion for the current outcomes.

### 3. Results and discussions

Semi-microscopic investigation of the elastic scattering angular distributions of  $^{10}\text{C}$  projectile on  $^4\text{He}$ ,  $^{27}\text{Al}$ ,  $^{58}\text{Ni}$  and  $^{208}\text{Pb}$  targets at various energies was carried out using three distinct density distributions of  $^{10}\text{C}$  labeled as SPh, DHB and VMC. The radial shape of the three density distributions under consideration is depicted in Fig. 1, in linear and logarithmic scale. These densities are distinguished by a prolonged tail, which represents the unusual nature of  $^{10}\text{C}$ . However the SPh has the greatest value in the center and the longest tail as the radius increases when compared to the others.

Figure 2 represents the different calculated potentials of  $^{10}\text{C} + ^{208}\text{Pb}$  system at  $E_{lab} = 256$  MeV. Moreover, the generated real CF potentials for the considered systems:  $^{10}\text{C} + ^4\text{He}$ ,  $^{10}\text{C} + ^{27}\text{Al}$ ,  $^{10}\text{C} + ^{58}\text{Ni}$  and  $^{10}\text{C} + ^{208}\text{Pb}$  are shown in Fig. 3. As shown in Fig. 2 (upper panel), the real folded potentials employing the CDM3Y6-RT interaction + SPh, DHB, and VMC densities exhibit comparable behavior and considerable variances in depth values in comparison to the SPP and CFP + DHB potentials. This is due to the difference in the direct and exchange terms of real potentials in presence of the RT term. However, as demonstrated in Fig. 2 (lower panel), there are minor variations when CDM3Y6 interaction is used in conjunction with SPP and CFP + DHB potentials.

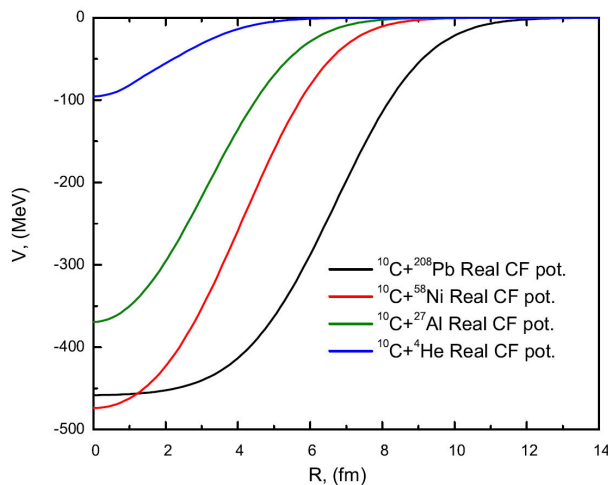


FIGURE 3. The prepared real CF potentials for  $^{10}\text{C} + ^4\text{He}$ ,  $^{10}\text{C} + ^{27}\text{Al}$ ,  $^{10}\text{C} + ^{58}\text{Ni}$  and  $^{10}\text{C} + ^{208}\text{Pb}$  implemented in CFOM calculations.

Furthermore, the CDM3Y6/RT + SPh potentials have the shallowest potentials depth and the SPP + DHB potential has the deepest. Mainly, these behaviors are repeated for all the investigated systems at different energies.

The semi-microscopic potential of Eq. (3) is used to calculate the impact of the density distribution in conjunction with the considered  $NN$  effective interactions. The real part of the potential is calculated using the CDM3Y6 and CDM3Y6-RT effective  $NN$  interactions folded with SPh, DHB and VMC densities, as well as SP and CFP folded with DHB density within REGINA code [22]. Hence, eight microscopic real potentials are obtained according to the different (interaction potential + densities) combinations, namely, CDM3Y6 + DHB, CDM3Y6-RT + DHB, SPP + DHB, CDM3Y6 + SPh, CDM3Y6-RT + SPh, CDM3Y6 + VMC, CDM3Y6-RT + VMC, and CFP + DHB, which are implemented in the calculations. This folding technique is distinguished by an adjustable parameter  $N_R$ , which is the renormalization factor for the implemented real microscopic DF potential. This factor is allowed to be freely changed till the best agreement between experimental data and theoretical calculations is reached through minimizing the  $\chi^2$  values. The created real microscopic potentials are then multiplied by the  $N_R$  factor, hence increasing or decreasing the prepared potentials' strength. Then, and by using an appropriate search code such as SFRESCO [56] and HIOPTM-94 [61], we could get the optimal  $N_R$  value. Of course, as the value of this factor ( $N_R$ ) is close to unity, it means that the used potential is non-renormalized.

The value of  $N_R$  is set to unity by default. The variation from this number, however, might be attributed to the ambiguities or peculiarities in experimental data or the fitting process of theoretical calculations. In addition to the  $N_R$ , the potential parameters which characterize the imaginary parts

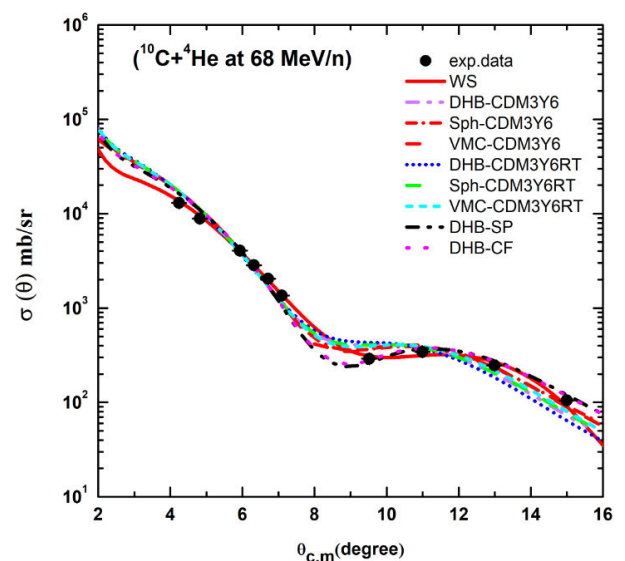


FIGURE 4. Comparison between the experimental angular distributions for  $^{10}\text{C}$  elastically scattered on  $^4\text{He}$  at  $E_{lab} = 68$  MeV/n and the theoretical OM calculations.

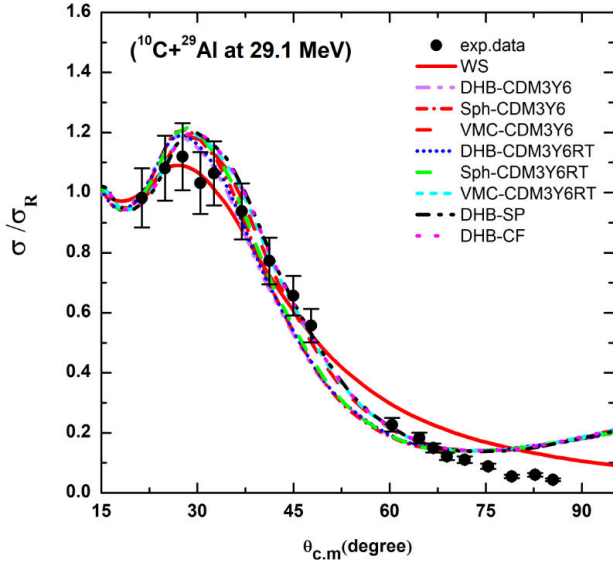


FIGURE 5. Same as Fig. 4 but for  $^{10}\text{C}$  elastically scattered on  $^{27}\text{Al}$  at  $E_{lab} = 29.1$  MeV.

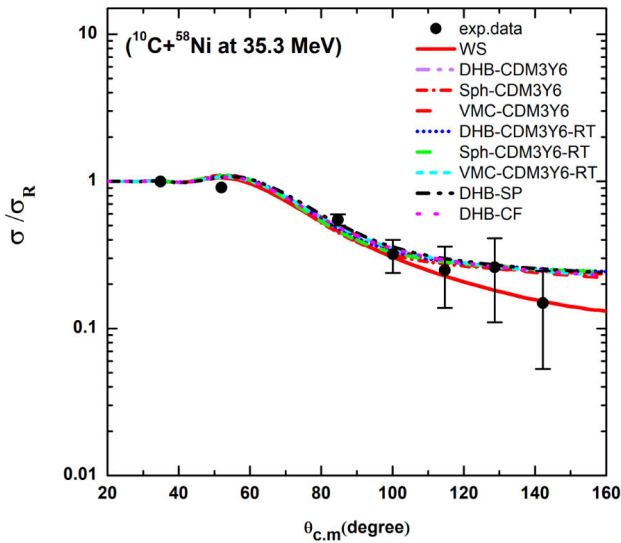


FIGURE 6. Same as Fig. 4 but for  $^{10}\text{C}$  elastically scattered on  $^{58}\text{Ni}$  at  $E_{lab} = 35.3$  MeV.

of the OP ( $W_0$ ,  $r_W$ ,  $a_W$ ), as expressed in Eqs. (3) and (18), are allowed to change till the best fit to data is achieved. As demonstrated in Figs. 4–9, the free parameters are changed to yield findings that are in good agreement with the experimental data. However, we attempted to achieve the best fit in the forward region at an angle between ( $25^\circ$ – $45^\circ$ ) as shown in Fig. 5, and this is reflected in an overestimation of the data in the tail at an angle between ( $65^\circ$ – $85^\circ$ ) and a lower chi-squared value rather than an underestimation as in Aguilera *et al.*, [49] Thus, chi squared = 17.1 is obtained using  $N_R = 1.25$  and the fitted WS parameters in our work, whereas chi squared = 24.7 is obtained using  $N_R = 1$  and the WS parameters of Aguilera *et al.*

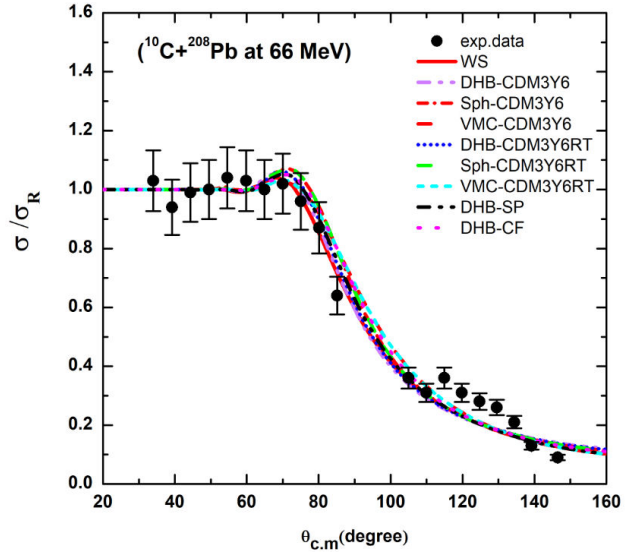


FIGURE 7. Same as Fig. 4 but for  $^{10}\text{C}$  elastically scattered on  $^{208}\text{Pb}$  at  $E_{lab} = 66$  MeV.

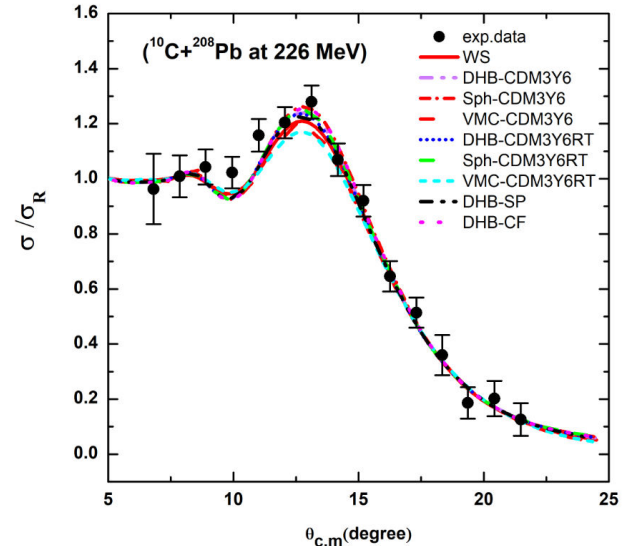


FIGURE 8. Same as Fig. 4 but for  $^{10}\text{C}$  elastically scattered on  $^{208}\text{Pb}$  at  $E_{lab} = 226$  MeV.

Tables I and II show the values obtained for each reaction. Furthermore, phenomenological analysis was performed on the same set of reactions, with the phenomenological WS form being used for both real and imaginary OP portions. The free parameters are varied to provide findings that are in excellent agreement with the experimental data. The angular distributions predictions are provided in the same Figs. 4–9 for the sake of comparison, and the obtained parameters are also documented in Tables I and II.

Tables I and II demonstrate that the findings are highly sensitive to the extracted  $N_R$  value which ranges between 0.48 and 1.25. In general, the  $N_R$  values of CDM3Y6/RT + DHB are lower than those of other combinations. This is consistent with the reported results for the neutron-rich  $^{11}\text{Li}$  projectile nucleus (given in Tables IV and V) in Ref. [29].

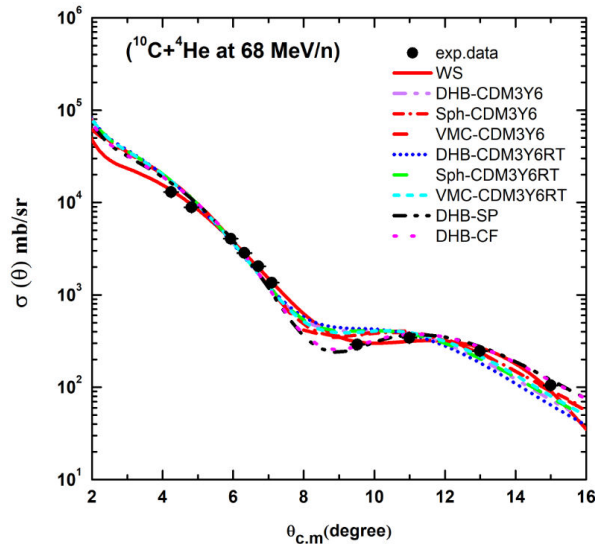


FIGURE 9. Same as Fig. 4 but for  $^{10}\text{C}$  elastically scattered on  $^{208}\text{Pb}$  at  $E_{lab} = 256$  MeV.

Furthermore, the outcomes of SPP + DHB and CDM3Y6/RT + VMC achieved with  $N_R \approx 1$  in case of considered high energies (680, 256, 226 and 66 MeV) and  $N_R=1$  for CFP + DHB in case of low energies (29.1 and 35.3 MeV). In other words, these data is described using a non-renormalized ( $N_R=1$ ) real folded potential, which consequently gives an evidence for the success of the used microscopic real potentials.

As demonstrated in Figs. 4–9, all of the computed OPs with free one real parameter  $N_R$  in addition to three imaginary WS free parameters generated almost identical behaviour to experimental data for each reaction at corresponding energy. In terms of  $^{10}\text{C}$  densities distributions sensitivity, it is obvious that the  $N_R$  and  $W_0$  parameters may compensate for any of them. Again, the  $\chi^2/N$  values of  $^4\text{He}$  at 680 MeV and  $^{208}\text{Pb}$  at 226 and 256 MeV (far over the barrier) are considerably less than those at lower energies (close to the barrier), indicating strong agreement between the estimated scattering cross sections and experimental data. As an upshot, discrepancy between theory and experiment is found for  $^{27}\text{Al}$ ,  $^{58}\text{Ni}$  and  $^{208}\text{Pb}$  at energies 29.1, 35.3 and 66 MeV (close to the barrier), respectively, especially at large angles associated by high  $\chi^2/N$  values. In this context, the same observations have been reported in Refs. [47-51,62,63]. The neglect of transferring nucleon from projectile to the target during the breakdown process might be the cause of the discrepancy, as stated in Ref. [28,64] for  $^8\text{B}+^{58}\text{Ni}$  at energy range 20.7–29.3 MeV. It is worth mentioning that all the considered systems are reanalyzed at energies well above the Coulomb barrier. The interaction dynamics may greatly differ as the bombarding energies become close to and below the Coulomb barrier. Our forthcoming work will discuss the peculiarities of interaction at lower energies (close to the Coulomb barrier energy) as well as observe the transfer, breakup, and other mechanisms which could affect the reaction channels.

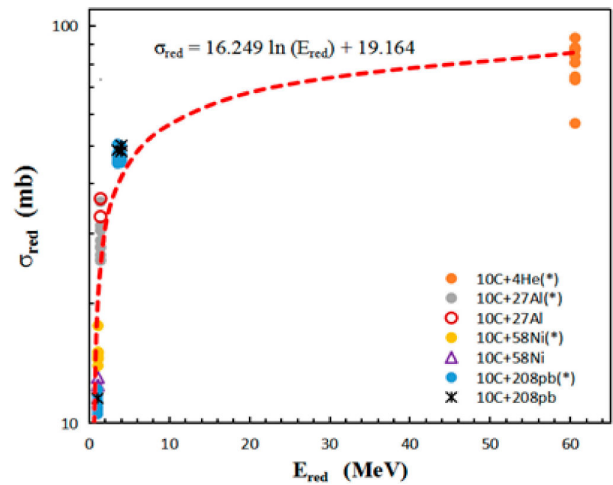


FIGURE 10. Reduced reaction cross section for several projectiles on ( $^4\text{He}$ ,  $^{27}\text{Al}$ ,  $^{58}\text{Ni}$  and  $^{208}\text{Pb}$ ) targets [21,39,40,49,51,63,65,67-72]. The general trend of ( $^{10}\text{C} + ^4\text{He}$ ,  $^{27}\text{Al}$ ,  $^{58}\text{Ni}$  and  $^{208}\text{Pb}$ ) systems is represented by the dashed line of indicated logarithmic formula. For the systems indicated by asterisk symbol (\*), the reaction cross section is obtained in the present work.

Tables I and II also provide the reaction cross section ( $\sigma_R$ ) values for all potentials used. The  $\sigma_R$  values of semi-microscopic potentials are observed to be in agreement with each other for each reaction at associated energy. Whereas, with the exception of the  $^{10}\text{C} + ^4\text{He}$  system, greater  $\sigma_R$  values are obtained from phenomenological WS potentials in comparison with those obtained from semi-microscopic potentials. This result is agreeable with that gained by authors of Ref. [44]. For comparison with literature, the  $\sigma_R$  values of  $^{10}\text{C} + ^{208}\text{Pb}$  reaction at 66 MeV as 793.2, and 703.9 mb for WS and CF potentials are agreeable with 753, 699 mb for WS and coupled potentials (for  $^{10}\text{C}$  cluster form as  $^9\text{B} + p$ ) calculations [51], respectively. Also, the extracted  $\sigma_R$  values of the same reaction at 226 and 256 MeV are 3360, 3352, 3269, 3178 mb for WS and SP potentials, severally, close to those reported in Ref. [50] by using WS and SP potentials. Somewhat, the deduced  $\sigma_R$  values for  $^{10}\text{C} + ^{27}\text{Al}$ ,  $^{58}\text{Ni}$  reactions are different with respect to the published data [63,65]. This could originate from the unlike models used in analysis.

A commonly utilized reduction approach [66] was employed to clarify the comparison of total reaction cross sections for the systems under consideration. The cross section is scaled as  $\sigma_R / (A_P^{1/3} + A_T^{1/3})^2$  and energy is scaled as  $E_{c.m.} (A_P^{1/3} + A_T^{1/3}) / (Z_P Z_T)$ . The symbols  $P$  and  $T$  refer to projectile and target respectively,  $\sigma_R$  denotes the total reaction cross section,  $Z$  denotes the charge, and  $A$  denotes the masses of the involved nuclei. The typical geometrical and charge differences between reaction systems were therefore suitably reduced while the dynamical effects of interest were not washed out. The variance in reduced reaction cross sections ( $\sigma_{red.}$ ) derived in this study from different potentials calculations at different reduced energies ( $E_{red.}$ ) for the  $^{10}\text{C} + ^4\text{He}$ ,  $^{27}\text{Al}$ ,  $^{58}\text{Ni}$  and  $^{208}\text{Pb}$  systems, as well as comparisons with previously published values in the literature, is shown in

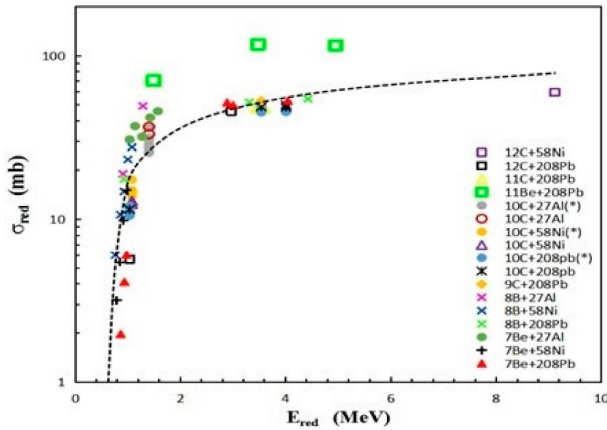


FIGURE 11. Same as Fig. 10 but the dashed line is to guide the eye for clarifying the general behavior for all systems. Note that, ignoring the data for  $^{10}\text{C} + ^4\text{He}$  system is due to the lack of other data for comparability at low energies.

Fig. 10. The results for various potentials are close to each other and correspond well with previously published values [21,49,51,63,65]. The energy dependency on reaction cross sections is depicted in the figure by the trend line of a logarithmic formula:  $\sigma_{\text{red}} = 16.249 \ln(E_{\text{red}}) + 19.164$  MeV. Furthermore, the findings presented in Fig. 11 incorporate systems of various light projectiles on the same regarded targets as those used in the current work. The  $\sigma_R$  values were derived from references [39,40,67-72]. At energies close to the barrier, lighter mass projectiles have a mass dependent cross section. To rationalize this conclusion, systems with exotic nuclei ( $^{11}\text{Be}$  and  $^8\text{B}$ ) are expected to have a greater breakup likelihood than weakly and tightly bound nuclei ( $^7\text{Be}$  and  $^{9-12}\text{C}$ ) at energies around the barrier, resulting in greater reaction cross sections. This is ascribable to the difference in their binding energies. At energies above the barrier, the  $\sigma_{\text{red}}$  for systems involve ( $^8\text{B}$ ,  $^7\text{Be}$ ,  $^{9-12}\text{C}$ ) are almost identical. However, the  $\sigma_{\text{red}}$  for the nucleus  $^{11}\text{Be}$  are obviously larger than other nuclei at the same conditions. As a result,  $^{11}\text{Be}$  (neutron halo) has a significant contribution to other channels than  $^8\text{B}$  (proton halo) at such considered high incident energies as mentioned in Ref. [68]. This general trend is similar to that prevailed in Refs. [51,68,73].

It is also worth noting that the real volume integrals  $J_R$  of the resulting potentials are affected by the density distributions under considerations as are the imaginary volume integrals  $J_I$ . Unfortunately, this analysis of the four investigated systems at different energies does not show a comprehensible performance concerning the  $J_R$  and  $J_I$  variation as a function of incident energy or target mass number. Merely, it is marked that the  $J_R$  values decrease as energy increases for the systems include  $^{208}\text{Pb}$  target nucleus. On contrary, the

values of the  $J_R$  increase and  $J_I$  decrease as energy increases for the same systems analyzed using the phenomenological WS potentials.

## 4. Conclusion

The  $^{10}\text{C} + ^4\text{He}$ ,  $^{10}\text{C} + ^{27}\text{Al}$ ,  $^{10}\text{C} + ^{58}\text{Ni}$  and  $^{10}\text{C} + ^{208}\text{Pb}$  angular distributions in the energy range 29.1–256 MeV are investigated utilizing different approaches. The OM analysis using nuclear potential consisting of two parts – real and imaginary volume terms each of WS shape was successful in reproducing the considered data. Then the concerned data is analyzed using different microscopic real potential created based on CDM3Y6 and CDM3Y6-RT interactions as well as SP and CF potentials in addition to an imaginary part taken as a WS form. The different four interaction potentials, namely, CDM3Y6, CDM3Y6-RT, SPP, and CFP combined with three different  $^{10}\text{C}$  densities, namely, SPh, DHB and VMC, forming eight different combinations of interaction potential + density, namely, CDM3Y6 + DHB, CDM3Y6-RT + DHB, SPP + DHB, CDM3Y6 + SPh, CDM3Y6-RT + SPh, CDM3Y6 + VMC, CDM3Y6-RT + VMC, and CFP + DHB approaches. The eight adopted combinations of potentials give equally good fitting for the considered data. In terms of renormalization factors for the different combinations, the average extracted renormalization factors from the analysis of the considered systems are:  $0.68 \pm 0.16$ ,  $0.72 \pm 0.19$ ,  $1.1 \pm 0.1$ ,  $0.79 \pm 0.19$ ,  $0.84 \pm 0.23$ ,  $0.95 \pm 0.17$ ,  $0.98 \pm 0.14$ , and  $0.92 \pm 0.06$  for the approaches CDM3Y6 + DHB, CDM3Y6-RT + DHB, SPP + DHB, CDM3Y6 + SPh, CDM3Y6-RT + SPh, CDM3Y6 + VMC, CDM3Y6-RT + VMC, CFP + DHB, respectively. The performed analysis using SPP + DHB, CDM3Y6 + VMC, CDM3Y6-RT + VMC and CFP + DHB approaches are the best, as the extracted  $N_R$  values are very close to 1. While, the performed analysis using CDM3Y6 + DHB, CDM3Y6-RT + DHB, CDM3Y6 + SPh, CDM3Y6-RT + SPh approaches require a reduction in potential strength by  $\sim 32\%$ ,  $28\%$ ,  $21\%$ , and  $16\%$ , respectively. The behavior of energy dependence on reaction cross sections is studied and it agrees well with neighboring systems.

## Acknowledgement

Awad Ibraheem extend his appreciation to the Deanship of Scientific Research at King Khalid University for funding this work through research groups program under grant number R.G.P.2/102/143 .Sh. Hamada is funded by a full post-doctoral scholarship from the Ministry of Higher Education of the Arab Republic of Egypt.

1. G. R. Satchler and W. G. Love, *Folding model potentials from realistic interactions for heavy-ion scattering*, *phys. Rep.* **55** (1979) 183, [https://doi.org/10.1016/0370-1573\(79\)90081-4](https://doi.org/10.1016/0370-1573(79)90081-4).
2. R. J. Woolliscroft *et al.*, *Elastic scattering and fusion of  $^9\text{Be} + ^{208}\text{Pb}$ : Density function dependence of the double folding renormalization*, *Phys. Rev. C* **69** (2004) 044612, <https://doi.org/10.1103/Phys.Rev.C.69.044612>.
3. M. Aygun and I. Boztosun, *An Extended Analysis of the Elastic Scattering of  $^6\text{Li}$  ( $^6\text{He}$ ,  $^6\text{He}$ )  $^6\text{Li}$  system at 17.9 MeV*, *Few-Body Syst.* **55** (2014) 203, <https://doi.org/10.1007/s00601-014-0856-9>.
4. M. Aygun, *Folding Model Analysis of Elastic Scattering of  $^{11}\text{B}$  from Light, Medium, and Heavy Nuclei*, *Commun.Theor.Phys.* **66** (2016) 531, <https://doi.org/10.1088/0253-6102/66/5/531>.
5. M. Aygun, O. Kocadag and Y. Sahin, *Phenomenological and microscopic analysis of elastic scattering reactions of  $^{18}\text{O}$  by  $^{24}\text{Mg}$ ,  $^{28}\text{Si}$ ,  $^{58}\text{Ni}$ ,  $^{64}\text{Zn}$ ,  $^{90}\text{Zr}$ ,  $^{120}\text{Sn}$  and  $^{208}\text{Pb}$  target nuclei*, *Rev.Mex.Fis.* **61** (2015) 414, <https://www.scielo.org.mx/pdf/rmf/v61n6/v61n6a2.pdf>.
6. F. S. Olise *et al.*, *Response of multi-step compound pre-equilibrium reaction cross sections for the (p, n) reactions to forms of optical model parameters*, *Nucl.Sci.Tech.* **28** (2017) 147, <https://doi.org/10.1007/s41365-017-0298-4>.
7. G. F. Bertsch, J. Borysowicz, H. Mcmanus and W. G. Love, *Interactions for inelastic scattering derived from realistic potentials*, *Nucl. Phys. A* **284** (1977) 399, [https://dx.doi.org/10.1016/0375-9474\(77\)90392-x](https://dx.doi.org/10.1016/0375-9474(77)90392-x).
8. M. El-Azab Farid and G. R. Satchler, *A density-dependent interaction in the folding model for heavy-ion potentials*, *Nucl. Phys. A* **438** (1985) 525, [https://doi.org/10.1016/0375-9474\(85\)90391-4](https://doi.org/10.1016/0375-9474(85)90391-4).
9. Z. Majka, H. J. Gils, H. Rebel, *Cluster folding model for  $^{12}\text{C}$  ( $^6\text{Li}$ ,  $^6\text{Li}$ )  $^{12}\text{C}$  scattering at 156 MeV*, *Phys. Rev. C* **25** (1982) 2996, <https://doi.org/10.1103/PhysRevC.25.2996>.
10. E. Crema, P. R. S. Gomes and L. C. Chamon, *Appropriate bare potentials for studying fusion induced by  $^6\text{He}$* , *Phys. Rev. C* **75** (2007) 037601, <https://doi.org/10.1103/PhysRevC.75.037601>.
11. S. Watanabe, *High energy scattering of deuterons by complex nuclei*, *Nucl. Phys. A* **8** (1958) 484, [https://doi.org/10.1016/0029-5582\(58\)90180-9](https://doi.org/10.1016/0029-5582(58)90180-9).
12. J. W. Watson, *Optical potentials for the elastic scattering of  $^6\text{Li}$  ions*, *Nucl. Phys. A* **198** (1972) 129, [https://doi.org/10.1016/0375-9474\(72\)90775-0](https://doi.org/10.1016/0375-9474(72)90775-0).
13. J. R. Beene, D. J. Horen and G. R. Satchler, *On the hindrance of  $3^-$  excitations induced by nuclear scattering*, *Phys. Lett. B* **344** (1995) 67, [https://doi.org/10.1016/0370-2693\(94\)01537-M](https://doi.org/10.1016/0370-2693(94)01537-M); *Critical comparison of folded potential and deformed potential models of heavy-ion inelastic scattering*, *Nucl. Phys. A* **596** (1996) 137, [https://doi.org/10.1016/0375-9474\(95\)00385-1](https://doi.org/10.1016/0375-9474(95)00385-1).
14. M. E. Brandan and G. R. Satchler, *The interaction between light heavy-ions and what it tells us*, *Phys. Rep.* **285** (1997) 142, [https://doi.org/10.1016/S0370-1573\(96\)00048-8](https://doi.org/10.1016/S0370-1573(96)00048-8).
15. M. El-Azab Farid and M. A. Hassanain, *Density-independent folding analysis of the  $^{6,7}\text{Li}$  elastic scattering at intermediate energies*, *Nucl. Phys. A* **678** (2000) 38, [https://doi.org/10.1016/S0375-9474\(00\)00313-4](https://doi.org/10.1016/S0375-9474(00)00313-4); *Folding model analysis of  $^{6,7}\text{Li}$  elastic scattering at 12.5-53 MeV/u*, *Nucl. Phys. A* **697** (2002) 183-205, [https://doi.org/10.1016/S0375-9474\(01\)01244-1](https://doi.org/10.1016/S0375-9474(01)01244-1).
16. M. El-Azab Farid and M. A. Hassanain, *Folding model and coupled-channels analysis of  $6,7\text{Li}$  elastic and inelastic scattering*, *Eur. Phys. J. A* **19** (2004) 231, <https://doi.org/10.1140/epja/i2003-10122-3>.
17. M. El-Azab Farid, *Microscopic description of  $^4\text{He} + ^4\text{He}$  elastic scattering over the energy range  $E=100 - 280$  MeV*, *Phys. Rev. C* **74** (2006) 064616, <https://doi.org/10.1103/PhysRevC.74.064616>.
18. Z. Long, L. Hao and L. X. Yun, *Nucleon-nucleon interactions in the double folding model for fusion reactions*, *Chin. Phys. B* **18** (2009) 136, <https://doi.org/10.1088/1674-1056/18/1/021>.
19. D. T. Khoa, G. R. Satchler and W. von Oertzen, *Nuclear incompressibility and density dependent NN interactions in the folding model for nucleus-nucleus potentials*, *Phys. Rev. C* **954** (1997) 56, <https://doi.org/10.1103/PhysRevC.56.954>.
20. D. T. Khoa, N. H. Phuc, D. T. Loan and B. M. Loc, *Nuclear mean field and double-folding model of the nucleus-nucleus optical potential*, *Phys. Rev. C* **94** (2016) 034612, <https://doi.org/10.1103/PhysRevC.94.034612>.
21. L. C. Chamon *et al.*, *Toward a global description of the nucleus-nucleus interaction*, *Phys. Rev. C* **66** (2002) 014610, <https://doi.org/10.1103/PhysRevC.66.014610>.
22. L. C. Chamon, B. V. Carlson and L. R. Gasques, *Sao Paulo potential version 2 (SPP2) and Brazilian nuclear potential (BNP)*, *Comp. Phys. Comm.* **267** (2021) 10806, <https://doi.org/10.1016/j.cpc.2021108061>.
23. X. Chen, Y. W. Lui, H. L. Clark, Y. Tokimoto and D. H. Youngblood, *Giant resonances in  $^{24}\text{Mg}$  and  $^{28}\text{Si}$  from 240 MeV  $^6\text{Li}$  scattering*, *Phys. Rev. C* **80** (2009) 014312, <https://dx.doi.org/10.1103/PhysRevC.80.014312>.
24. Krishichayan, X. Chen, Y. W. Lui, J. Button and D. H. Youngblood, *Elastic and inelastic scattering of 240-MeV  $^6\text{Li}$  ions from  $^{40}\text{Ca}$  and  $^{48}\text{Ca}$  and tests of a systematic optical potential*, *Phys. Rev. C* **81** (2010) 044612, <https://doi.org/10.1103/PhysRevC.81.044612>.
25. L. C. Chamon, L. R. Gasques, *Reinterpreting the energy dependence of the optical potential*, *J. Phys. G* **43** (2016) 015107, <https://dx.doi.org/10.1088/0954-3899/43/1/015107>.
26. Sunday D. Olorunfunmi and Armand Bahini, *Reanalysis of  $^{10}\text{B} + ^{120}\text{Sn}$  Elastic Scattering Cross Section Using SAo Paulo Potential Version 2 and Brazilian Nuclear Potential*, *Braz. J. Phys.* **52** (2022) 11, <https://doi.org/10.1007/s13538-021-01018-y>.

27. K. O. Behairy *et al.*, *Analysis of strong refractive effect within  $^{11}\text{Li}$  projectile structure*, Chinese Phys. C **45** (2021) 024101, <https://doi.org/10.1088/1674-1137/abca1b>.
28. M. Anwar, Bodor El-Naggar and Kassem O. Behairy, *Microscopic Analysis of the  $^8\text{B} + ^{58}\text{Ni}$  Elastic Scattering at Energies from 20.7 to 29.3 MeV*, J. Phys. Soc. Jpn **91** (2022) 014201, <https://doi.org/10.7566/JPSJ.91.014201>.
29. M. Anwar, *Semimicroscopic analysis of  $^6\text{Li}$  elastic scattering at 40 MeV/nucleon*, Phys. Rev. C **101** (2020) 064617, <https://doi.org/10.1103/PhysRevC.101.064617>.
30. L. Y. Hu, Y. S. Songa and Y. W. Hou, H. L. Liu, *The cluster folding model analysis for the elastic scattering of  $^6\text{Li}$  and  $^6\text{He}$  on  $^{12}\text{C}$* , Eur. Phys. J. A **54** (2018) 230, <https://doi.org/10.1140/epja/i2018-12668-1>.
31. Sh. Hamada, I. Bondok and M. Abdelmoatmed, *Double Folding Potential of Different Interaction Models for  $^{16}\text{O} + ^{12}\text{C}$  Elastic Scattering*, Braz. J. Phys. **46**(2016) 740, <https://doi.org/10.1007/s13538-016-0450-3>.
32. Sh. Hamada *et al.*, *Analysis of  $^6\text{Li} + ^{16}\text{O}$  elastic scattering using different potentials*, Rev. Mex. Fis **66**(3) (2020) 322, <https://doi.org/10.31349/RevMexFis.66.322>.
33. M. Karakoc and I. Boztosun,  $\alpha - \alpha$  double folding cluster potential description of the  $^{12}\text{C} + ^{24}\text{Mg}$  system, Phys. Rev. C **73** (2006) 047601, <https://doi.org/10.1103/PhysRevC.73.047601>.
34. Y. X. Yang and Q. R. Li, *Elastic  $^{16}\text{O} + ^{20}\text{Ne}$  scattering from a folding model analysis*, Phys. Rev. C **84** (2011) 014602, <https://doi.org/10.1103/PhysRevC.84.014602>.
35. M. El-Azab Farid *et al.*, *Alpha-deuteron (triton) analysis of  $^{6,7}\text{Li}$  elastic scattering*, J. Phys. G: Nucl. Part. Phys. **40** (2013) 075108, <https://doi.org/10.1088/0954-3899/40/7/075108>.
36. P. R. S. Gomes *et al.*, *Fusion, break-up and elastic scattering of weakly bound nuclei*, J. Phys. G: Nucl. Part. Phys. **31** (2005) S1669, <https://doi.org/10.1088/0954-3899/31/10/051>.
37. M. S. Hussein, P. R. S. Gomes, J. Lubian and L. C. Chamon, *New manifestation of the dispersion relation: Breakup threshold anomaly*, Phys.Rev.C **73** (2006) 044610, <https://doi.org/10.1103/PhysRevC.73.044610>.
38. A. Gómez Camacho, E. F. Aguilera, P. R. S. Gomes and J. Lubian, *Breakup threshold anomaly for the  $^8\text{B} + ^{58}\text{Ni}$  system at near-Coulomb barrier energies*, Phys.Rev.C **84** (2011) 034615, <https://doi.org/10.1103/PhysRevC.84.034615>.
39. M. Mazzocco *et al.*, *Elastic scattering for the  $^8\text{B}$  and  $^7\text{Be} + ^{208}\text{Pb}$  systems at near-Coulomb barrier energies*, Phys. Rev. C **100** (2019) 024602, <https://doi.org/10.1103/PhysRevC.100.024602>.
40. E. F. Aguilera *et al.*, *Reaction cross sections for  $^8\text{B}$ ,  $^7\text{Be}$ , and  $^6\text{Li} + ^{58}\text{Ni}$  near the Coulomb barrier: Proton-halo effects*, Phys. Rev. C **79** (2009) 021601(R), <https://doi.org/10.1103/PhysRevC.79.021601>.
41. M. A. Nagarajan, C. C. Mahaux and G. R. Satchler, *Dispersion Relation and the Low-Energy Behavior of the Heavy-Ion Optical Potential*, Phys. Rev. Lett. **54** (1985)1136, <https://doi.org/10.1103/PhysRevLett.54.1136>.
42. G. R. Satchler, *Heavy-ion scattering and reactions near the Coulomb barrier and threshold anomalies*, Phys. Rep. **199** (1991) 147, [https://doi.org/10.1016/0370-1573\(91\)90066-U](https://doi.org/10.1016/0370-1573(91)90066-U).
43. V. Guimarães *et al.*, *Role of cluster configurations in the elastic scattering of light projectiles on  $^{58}\text{Ni}$  and  $^{64}\text{Zn}$  targets: a phenomenological analysis*, Eur. Phys. J. A **57** (2021) 90, <https://doi.org/10.1140/epja/s10050-021-00403-0>.
44. Awad A. Ibraheem and M. Aygun, *An Investigation of  $^{10,11}\text{Be} + ^{64}\text{Zn}$  Reactions Using Different Potentials*, Phys. Atom. Nuclei **81** (2018) 714, <https://doi.org/10.1134/S1063778818060194>.
45. C. Liang and K. Mislow, *On Borromean links*, J Math Chem **16** (1994) 27, <https://doi.org/10.1007/BF01169193>.
46. N. Curtis *et al.*, *Breakup reaction study of the Brunnian nucleus  $^{10}\text{C}$* , Phys. Rev. C **77** (2008) 021301(R), <https://doi.org/10.1103/PhysRevC.77.021301>.
47. T. Furuno *et al.*, *Neutron quadrupole transition strength in  $^{10}\text{C}$  deduced from the  $^{10}\text{C}(\alpha, \alpha)^{10}\text{C}$  measurement with the MAIKo active target*, Phys. Rev. C **100** (2019) 054322, <https://doi.org/10.1103/PhysRevC.100.054322>.
48. V. Guimarães *et al.*, *Strong coupling effect in the elastic scattering of the  $^{10}\text{C} + ^{58}\text{Ni}$  system near barrier*, Phys. Rev. C **100** (2019) 034603, <https://doi.org/10.1103/PhysRevC.100.034603>.
49. E. F. Aguilera *et al.*, *Elastic scattering of  $^{10}\text{C} + ^{27}\text{Al}$* , J. Phys.: Conf. Ser. **876** (2017) 012001, <https://doi.org/10.1088/1742-6596/876/1/012001>.
50. Y. Y. Yang *et al.*, *Quasi-elastic scattering of  $^{10,11}\text{C}$  and  $^{10}\text{B}$  from a nat Pb target*, Phys. Rev. C **90** (2014) 014606, <https://doi.org/10.1103/PhysRevC.90.014606>.
51. R. Linares *et al.*, *Elastic scattering measurements for the  $^{10}\text{C} + ^{208}\text{Pb}$  system at  $E_{\text{lab}} = 66$  MeV*, Phys. Rev. C **103** (2021) 044613, <https://doi.org/10.1103/PhysRevC.103.044613>.
52. A. Bhagwat, Y. K. Gambhir and S. H. Patil, *Nuclear densities in the neutron-halo region*, Eur. Phys. J. A **8** (2000) 511, <https://doi.org/10.1007/s100500070074>.
53. A. Bhagwat, Y. K. Gambhir and S. H. Patil, *Nuclear densities of Li isotopes*, J. Phys. G: Nucl. Part. Phys. **27** (2001) B1, <https://doi.org/10.1088/0954-3899/27/2/3b1>.
54. <https://www.phy.anl.gov/theory/research/density/>
55. N. Anantaraman, H. Toki and G. F. Bertsch, *An effective interaction for inelastic scattering derived from the Paris potential*, Nucl. Phys. A **398** (1983) 269, [https://doi.org/10.1016/0375-9474\(83\)90487-6](https://doi.org/10.1016/0375-9474(83)90487-6).
56. I.J. Thompson, *Coupled reaction channels calculations in nuclear physics*, Comput. Phys. Rep. **7** (1988)167, [https://doi.org/10.1016/0167-7977\(88\)90005-6](https://doi.org/10.1016/0167-7977(88)90005-6).
57. G. E. Thompson, M. B. Epstein, and T. Sawada, *Optical-model analysis of the scattering of protons from  $^4\text{He}$  at 31, 40, 46 and 55 MeV*, Nucl. Phys. A **142** (1970) 571, [https://doi.org/10.1016/0375-9474\(70\)90813-4](https://doi.org/10.1016/0375-9474(70)90813-4).

58. V. S. Prokopenko, V. V. Tokarevskii, and V. N. Shcherbin, *Elastic Scattering of Protons by Medium-Mass Nuclei*, *Izv.Akad.Nauk SSSR, Ser.Fiz.* **34** (1970) 126; *Bull.Acad.Sci.USSR, Phys. Ser.* **34** (1971) 116.
59. D. Hoare, A. B. Robbins and G. W. Greenlees, *Polarization of 9 MeV Protons Elastically Scattered from C and Al*, *Proc. Phys. Soc.* **77** (1961) 830, <https://doi.org/10.1088/0370-1328/77/4/303>.
60. W. T. H. Van Ores Huang Haw, *et al.*, *Optical-model analysis of  $p+^{208}\text{Pb}$  elastic scattering from 15 - 1000 MeV*, *Phys. Rev. C* **10** (1974) 307, <https://doi.org/10.1103/PhysRevC.10.307>.
61. N.M. Clarke, *Hi-Optim 94.2 Code (1994)* (University of Birmingham) unpublished
62. Y. Xu *et al.*, *Description of elastic scattering induced by the unstable nuclei  $^{9,11,13,14}\text{C}$* , *Chinese Phys. C* **45** (2021) 114103, <https://doi.org/10.1088/1674-1137/ac1fel>.
63. M. Aygun, *Comprehensive Research of  $^{10}\text{C}$  Nucleus Using Different Theoretical Approaches*, *Ukr.J.Phys.* **66** (2021) 653, <https://doi.org/10.15407/ujpe66.8.653>.
64. Y. Kucuk, V. Guimarães and B.V. Carlson, *Towards a systematic optical model potential for  $A = 8$  projectiles*, *Eur. Phys. J. A* **57** (2021) 87, <https://doi.org/10.1140/epja/s10050-021-00405-y>.
65. M. Aygun, *Analysis with relativistic mean-field density distribution of elastic scattering cross-sections of carbon isotopes ( $^{10-14,16}\text{C}$ ) by various target nuclei*, *Pramana J. Phys.* **93** (2019) 72, <https://doi.org/10.1007/s12043-019-1835-y>.
66. P. R. S. Gomes, J. Lubian, I. Padron and R. M. Anjos, *Uncertainties in the comparison of fusion and reaction cross sections of different systems involving weakly bound nuclei*, *Phys.Rev.C* **71** (2005) 017601, <https://doi.org/10.1103/PhysRevC.71.017601>.
67. S. R. Mokhtar, R. A. Abdel-Gahni, M. Tammam and M. El-Azab Farid, *Optical Model Analysis of  $^8\text{B}+^{27}\text{Al}$  Elastic Scattering Above the Coulomb Barrier*, *J. Rad. Nucl. Appl.* **3** (2018) 1-8, <https://dx.doi.org/10.18576/jrna/03010>.
68. F. F. Duan *et al.*, *Elastic scattering and breakup reactions of neutron-rich nucleus  $^{11}\text{Be}$  on  $^{208}\text{Pb}$  at 210 MeV*, *Phys.Rev.C* **105** (2022) 034602, <https://doi.org/10.1103/PhysRevC.105.034602>.
69. Y.Y. Yang *et al.*, *Elastic scattering of the proton drip line nuclei  $^7\text{Be}$ ,  $^8\text{B}$ , and  $^9\text{C}$  on a lead target at energies around three times the Coulomb barriers*, *Phys.Rev.C* **98** (2018) 044608, <https://doi.org/10.1103/PhysRevC.98.044608>.
70. Awad A.Ibraheem, M.El-Azab Farid and Arwa S.Al-Hajjaji, *Analysis of  $^8\text{B}$  Proton Halo Nucleus Scattered from  $^{12}\text{C}$  and  $^{58}\text{Ni}$  at Different Energies*, *Braz J Phys* **48** (2018) 507-512, <https://doi.org/10.1007/s13538-018-0586-4>.
71. K. Kalita *et al.*, *Elastic scattering and fusion cross sections for  $^7\text{Be}$ ,  $^7\text{Li}+^{27}\text{Al}$  systems*, *Phys.Rev.C* **73** (2006) 024609, <https://doi.org/10.1103/PhysRevC.73.024609>.
72. J. S. Wang *et al.*,  *$^7\text{Be}$ ,  $^8\text{B}+^{208}\text{Pb}$  Elastic Scattering at Above-Barrier Energies*, *J. of Phys.: Conference Series* **420** (2013) 012075, <https://doi.org/10.1088/1742-6596/420/1/012075>.
73. C. Joshi *et al.*, *Exploring breakup coupling effect in  $^7\text{Li} + ^{92,100}\text{Mo}$  elastic scattering around Coulomb barrier energies*, *Eur.Phys.J. A* **58** (2022) 40, <https://doi.org/10.1140/epja/s10050-022-00690-1>.